Revealing hot tearing mechanism for an additively manufactured high-entropy alloy via selective laser melting

Z. Sun, X.P. Tan, M. Descoins, Dominique Mangelinck, S.B. Tor, C.S. Lim

▶ **To cite this version:**

Z. Sun, X.P. Tan, M. Descoins, Dominique Mangelinck, S.B. Tor, et al.. Revealing hot tearing mechanism for an additively manufactured high-entropy alloy via selective laser melting. Scripta Materialia, 2019, 168, pp.129-133. ⟨10.1016/j.scriptamat.2019.04.036⟩. ⟨hal-02403163⟩

HAL Id: hal-02403163

https://hal.science/hal-02403163v1

Submitted on 14 Dec 2020

HAL is a multi-disciplinary open access archive for the deposit and dissemination of scientific research documents, whether they are published or not. The documents may come from teaching and research institutions in France or abroad, or from public or private research centers.

L'archive ouverte pluridisciplinaire **HAL**, est destinée au dépôt et à la diffusion de documents scientifiques de niveau recherche, publiés ou non, émanant des établissements d'enseignement et de recherche français ou étrangers, des laboratoires publics ou privés.

HAL Authorization

*Graphical Abstract

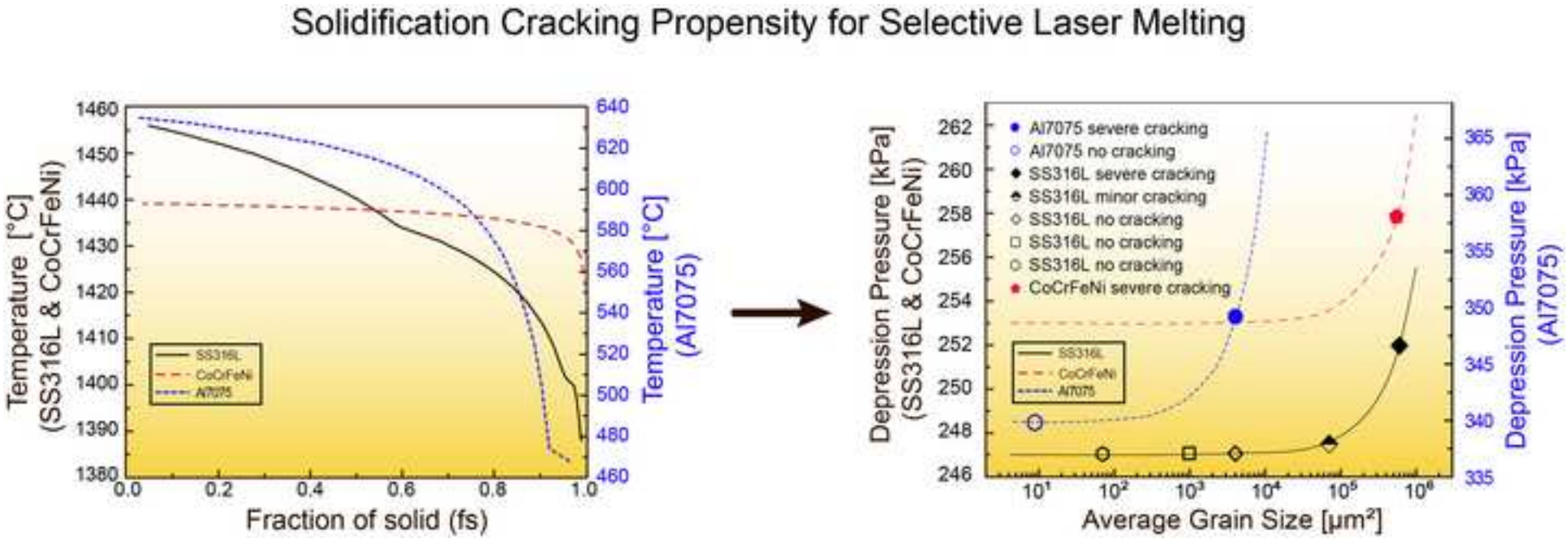

Revealing hot tearing mechanism for an additively manufactured high-entropy alloy via selective laser melting

Z. Sun[a], X.P. Tan[a,*], M. Descoins[b], D. Mangelinck[b], S.B. Tor[a,c], C.S. Lim[c]

[a]Singapore Centre for 3D Printing, School of Mechanical and Aerospace Engineering, Nanyang Technological University, 50 Nanyang Avenue, Singapore 639798

[b]IM2NP, UMR 7334 CNRS, Université Aix-Marseille, 13397 Marseille Cedex 20, France

[c]School of Mechanical and Aerospace Engineering, Nanyang Technological University, 50 Nanyang Avenue, Singapore 639798

*Corresponding author: xptan@ntu.edu.sg; +65 69082242

Abstract

Hot tearing mechanisms of a high-entropy alloy CoCrFeNi additively manufactured by selective laser melting have been investigated. Intergranular solidification cracks are present regardless of various parameters used, suggesting poor laser-based printability for the alloy. Elemental segregation does not exist at the grain boundary that favours the solidification cracking. We find that severe residual stress induced by the large grain size is the root cause for the intergranular cracking. The classic Rappaz-Drezet-Gremaud model is used to predict the characteristic depression pressure limit beyond which hot tearing will occur for the selective laser melting of metals and alloys.

Keywords: additive manufacturing; high-entropy alloy; laser deposition; hot tearing; solidification cracking

Belonging to the category of powder-bed fusion techniques for metal additive manufacturing (AM), Selective laser melting (SLM) has the unique advantages of producing parts with refined surface finish, having a wide material library and fabricating complex geometries [1]. Besides these benefits, it is also proven recently to have the potential of manufacturing components with superior mechanical properties as compared to its conventional counterparts [2-4]. However, despite the continuous efforts worldwide, feedstock used in SLM are predominantly comprised commercial engineering materials [1]. Material development catered to metal AM is still limited which has inevitably hindered its industrial applications. Therefore, it is imperative to deploy new metals and alloys for SLM process. High-entropy alloy (HEA) is a relatively new class of alloys which normally has multiple principal elements, usually 5 or more, in equimolar or near-equimolar ratios [5, 6].

Some HEAs have shown exceptional properties for cryogenic toughness [7] and strength-ductility combination [8]. CoCrFeNi-based alloys have been one of the most widely researched HEA series [9-12]. Hence, it is of great interest for both academy and industry to achieve high-quality printing of HEA materials via SLM.

Some CoCrFeNi based HEAs have been printed using SLM process [13-16]. However, it was found that under normal processing conditions, SLM-built CoCrFeNi exhibits poor tensile properties (e.g. ultimate tensile strength (UTS) is ~480 MPa and elongation is only ~ 8%) [13]. Carbon additions improved its UTS to ~800 MPa but the elongation was still below 15 %, as compared to the cast sample with an elongation of ~80% [9, 14]. For SLM-processed CoCrFeNiMn, hot isostatic pressing (HIP) was adopted to improve the densification [16]. All these suggest that HEAs might be susceptible to hot tearing or other build defects which was not paid enough attention by the previous studies. Lately, hot tearing phenomenon has increasingly been observed in metal AM. Though, most of the cases are confined to superalloys [17-19]. It is primarily due to the segregation induced precipitation and/or liquid film formation. Measures such as composition modifications and nano-particle additions were conducted to minimize the cracking [17, 20]. However, it is still unclear (i) to what extent hot tearing happens in SLM-built HEA, and (ii) what causes it to happen since HEA usually has single-phase microstructure. Both above-mentioned questions are critical towards improving the printability of HEAs in metal AM [21].

Gas atomized pre-alloyed equimolar CoCrFeNi powder (~20 to 63 μm) was used on SLM 250 HL system (SLM Solutions, Germany). To investigate the three-dimensional (3D) printability of the material, a wide range of processing parameters were tested. Firstly, by keeping the laser power constant, energy density was varied from 50 to 180 J/mm^3. 60 samples with various processing parameters were built. None of the samples has a relative build density higher than 99%. The optimal process parameter set holds a laser power of 150 W, hatch spacing of 100 μm, scanning speed of 270 mm/s and layer thickness of 50 μm. It generated a relative density of 98.7%. Secondly, two different scanning strategies, namely chessboard and stripe/bi-directional (illustrated in Fig. 1), with varying scanning lengths were deployed. For chessboard scanning strategy, laser scanning takes place randomly within the chessboard to minimize the residual stress. The representative SLM-built CoCrFeNi “C” sample (by chessboard scan) and “S” sample (by stripe scan) each has a strip size of 2.5 mm and 2 mm respectively.

Standard metallographic specimen preparation procedures for SLM-built stainless steel 316L (SS316L) were used on the HEA samples [22]. Optical microscopy (OM) and

scanning electron microscopy (SEM) were carried out on Zeiss Axioskop 2 Mat and JEOL 7600F, respectively. Electron backscatter diffraction (EBSD) was performed on the AZtecHKL Oxford system with a step size of 3 μm. The misorientation analysis was conducted via the MTEX software [23]. Tensile coupons were machined via electron discharge machining (EDM) to a gauge length of 10 mm and a cross section of 3 x 2 mm^2. The tensile testing was conducted on an Instron static tester (series 5569) with a strain rate of 1 x 10^4 s^{-1}. Contact based extensometer was used for the test. At least 3 sets of tests were conducted for each scanning strategy. Micro computed tomography (μ-CT) images was acquired using the Skyscan 1173 system (Bruker, Kontich, Belgium). A high voltage of 130 kV was used to achieve a resolution of ~6.4 μm. Atom probe tomography (APT) analysis was performed by LEAP 3000X HR (CAMECA, Gennevilliers, France). Focused ion beam (FIB) on a FEI Helios dual-beam was used for sample lift-out. The micro-tips with an end radius of ~50 nm were prepared using the annular milling method. Pandat software package and existing solidification data were used to generate the solidification paths of stainless steel 316L (SS316L), CoCrFeNi and Al7075 [20,24-25].

Fig. 1(a) and 1(b) display the cross-section images of the C and S samples along the build direction. The presence of cracks can be clearly noted. To reveal the detailed grain morphology, large-area EBSD scans with respect to the build direction were carried out. It is noted that the grain size of SLM-built CoCrFeNi samples is extraordinarily large, and columnar grains can epitaxially grow up to ~3 mm in length and ~200 μm in width. In comparison, SLM process typically generates a grain length of less than 0.1 mm for AlSi10Mg [26], and ~0.2 mm for SS316L, Inconel 625 and CoCrMo [4, 27, 28]. One close match is pure molybdenum with a grain length of ~2 mm, which also suffered from extensive intergranular cracking [29]. As known, lacking alloying content for grain nucleation will cause formation of big-sized grains in metals and alloys [30]. Thus, both CoCrFeNi and pure molybdenum might undergo limited constitutional undercooling during rapid solidification of AM process which leads to large columnar grains. Moreover, we found that epitaxial grain growth was broken down in the periphery of the lack-of-fusion cracks. However, small spherical pores circled in red have little influence on the grain growth. As observed by Leung et al. that spherical pores were mainly formed at the last stage of solidification due to the reduction of gas solubility as molten metals cooled down [31]. Therefore, epitaxial columnar grain growth is unlikely to be affected. Both samples exhibit a strong <011> crystallographic texture. By comparing the OM and EBSD images, ~70 cracks are randomly selected for misorientation computation. It is found out that all cracks are intergranular in nature and

majority of the adjacent grains' misorientations lies in between 40° to 50° (Supplementary Fig. 1).

Tensile testing results show that the yield strengths (Ys) are 556.7 ± 23.6 and 572 ± 7.48 MPa, the UTSs are 676.7 ± 20.5 and 691 ± 15.9 MPa, and the elongations are 12.4 ± 2.1% and 17.9 ± 0.9% for C and S samples respectively, which has shown to be superior to the previous work with the same layer thickness [13]. Moreover, S samples performed better with smaller deviations in terms of strength and ductility in comparison with C samples.

To elucidate the reasoning for the different mechanical performance of C and S samples, μ-CT data and the corresponding cross-sectional OM images are shown in Fig. 2(a) to 2(b). With the same scanning parameters but a different scanning strategy, C sample contains more cracks/pores compared to S sample. Moreover, for S sample, the cracks are randomly distributed which is a common phenomenon for metal AM fabricated parts [32]. However, for C sample, the cracks align themselves along the build direction. This phenomenon is validated in the OM images with the aligned cracks are circled in red. It is worth noting that the chimney-like cracks were only present under the chessboard scanning strategy with stripe sizes of 1.25 and 2.5 mm. It does not appear under the stripe scanning strategy (stripe sizes from 0.5 mm to 10 mm) nor the chessboard scanning strategy with a stripe size of 5 mm. For tensile fracture surfaces shown in Fig. 2(c) and 2(d), more elongated cracks are detected in C sample and they are believed to cause its property worsening and deviation. Hot tearing/solidification cracks are observed in both samples (Fig. 2(e) and 2(f)) showing typical protrusions with smooth surfaces [19].

It is reported that chemical heterogeneity at the high angle grain boundary helps to maintain the liquid film at the end of solidification, which causes solidification cracking of metal AM parts [19]. Elemental distribution in 3D form at atomic level was specifically conducted by means of APT technique near an intergranular crack as shown in Fig. 3(a). The APT tip specimen with a radius of ~50 nm was analysed (Fig. 3(b)). Fig. 3(c) reveals that distribution of the 4 constituting elements is uniform and their atomic ratios remain to be consistent. Obviously, no elemental segregation is seen at the intergranular crack. Thus, it is suggested that the solidification cracking could not be attributed to elemental segregation for this HEA.

Fig. 4(a) schematically illustrates a hot tearing mechanism in SLM process. As the liquid metal solidifies after the laser melting for each layer, cellular structures grow towards different directions within each grain. Residual stress ascribed to thermal shrinkage acts as a tension force perpendicular to the grain boundary. The unsolidified semi-solid metal tends to

fill up any open channel via gravity/capillary force, known as liquid feeding [33]. It is known that cracking susceptibility is related to the grain size for welding [34]. During solidification, grain boundaries are the weak "linkages" within the solid due to incoherent atomic packing. Therefore, under a uniform tensile force, fine-grained microstructure provides more grain boundaries to share the load and cracking is less likely to occur. Given the large grain size of SLM-built CoCrFeNi, there are fewer grain boundaries to withstand the residual stress. To assess the residual stress in the as-built CoCrFeNi samples, TEM studies were carried out. Fig. 4(b) shows a cellular structure in the <1-10> zone axis. The cell boundaries are marked by white arrows. Previously reported SLM-built cellular structures typically have a clean interior surrounded by dislocation cell boundaries [2]. However, the present as-built CoCrFeNi sample has dense entangled dislocations within the cell. It suggests that the SLM-built CoCrFeNi is under a high level of residual stresses.

To quantify the effect of grain size towards the hot tearing for the SLM processing of HEA, the Rappaz-Drezet-Gremaud (RDG) criterion is employed as it has been proven to be one of the most effective models in cracking susceptibility prediction [35]. The original RDG model considers the depression pressure Δp_{max} within the mushy zone induced by both solidification shrinkage (Δp_{sh}) and mechanical strain (Δp_{ε}) [36]:

$$\Delta p_{max} = \Delta p_{sh} + \Delta p_{\varepsilon} = \frac{180}{\lambda^2}\frac{(1+\beta)\mu}{G}\int_{T_S}^{T_L}\frac{E(T)f_s(T)^2}{\left(1-f_s(T)\right)^3}\,dT + \frac{180}{\lambda^2}\frac{v_T\beta\mu}{G}\int_{T_S}^{T_L}\frac{f_s(T)^2}{(1-f_s(T))^2}\,dT \quad (1)$$

with

$$E(T) = \frac{1}{G}\int f_s(T)\dot{\varepsilon}(T)\,dT,$$

whereas G is the thermal gradient, β is the shrinkage factor, μ is the dynamic viscosity, λ is the characteristic microstructural length, taken as the cellular structure width here, v_T is the solid-liquid front growth velocity, $f_s(T)$ is the solid fraction, $\dot{\varepsilon}$(T) is the strain rate, E(T) is the elongation and T_L is the liquidus temperature. T_S is the coherency temperature, below this value, liquid feeding problem becomes trivial as liquid film breaks down into isolated drops [36]. Though the RDG model was built without taking the grain boundary effects into consideration, Wang et al. successfully used it to explain the effect of grain boundary angle towards the laser-welding cracking susceptibility [37]. Therefore, the present study aims to establish a new set of characteristic depression pressure values Δp_{max} specifically for metal AM.

Unlike casting and welding, SLM involves an extremely high thermal gradient of ~10^6 K/m [26]. It makes the characteristic depression pressure Δp_{max} significantly higher compared to the conventional values. Like the original calculations made by the RDG model, the strain rate $\dot{\varepsilon}$ is assumed to be a constant value of 10^{-2} s^{-1} [36,38]. Due to the different nucleation tendencies and existing experimental data, it is assumed that for a cross-section normal to the build direction, the largest average grain size can be obtained for SLM-built CoCrFeNi, SS316L and Al7075 are 10^6, 10^6, and 10^4 μm^2 respectively [39,40]. To incorporate the effect of grain size, the strain rate $\dot{\varepsilon}$ is proportionally decreased as the lateral grain size decreases. Applying existing solidification path data (Fig. 4(c)) and their respective materials properties (Supplementary Table 1), we plot the depression pressure curves for CoCrFeNi, SS316L and Al7075, shown in Fig. 4(d). The coherency temperature T_S is taken as the temperature when $f_s(T)$ = 0.93 as suggested by [41]. Typically, Δp_{max} is inversely proportional to solidification temperature range. However, even with a short solidification range of ~20°C for CoCrFeNi, it still has a relatively high depression pressure Δp_{max} due to its high viscosity value of 3.15×10^{-2} $kgm^{-1}s^{-1}$ [42]. It is about 1 order of magnitude higher compared to the common alloys (Supplementary Table 1). It is observed that as the grain size decreases, the contribution of mechanical strain Δp_ε decreases exponentially. By substituting in the existing experimental data, it is found that once the corresponding grain size exceeds a characteristic depression pressure value, solidification cracking will start to occur. It is worth noting that, when the grain size is close to the transition point, only minor cracking appeared (Supplementary Fig. 2(a)). Based on the above-mentioned results, it is conceived that hot tearing for the SLM-built CoCrFeNi could be overcome when its average grain size is below 10^4 μm^2. Therefore, the focus of our future work will be refining the microstructure so as to conquer the hot tearing issue for AM processing of various HEAs.

In summary, this work revealed the origin of hot tearing for a HEA CoCrFeNi additively manufactured by SLM process. A wide range of processing parameters were implemented on pre-alloyed powder, but intergranular solidification cracks were present throughout the builds. The 4 constituting elements were found to be uniformly distributed on the periphery of cracks, which means that elemental segregation induced thin film of liquid may not be the reason for the hot tearing of this alloy. It is found out that severe residual stress due to the formation of large grains is the root cause and there will be a characteristic depression pressure limit beyond which solidification cracking tends to occur.

Acknowledgements

The authors are grateful for the use of resources in Singapore Centre for 3D Printing funded by the National Research Foundation (NRF), Singapore.

References

[1] T. DebRoy, H.L. Wei, J.S. Zuback, T. Mukherjee, J.W. Elmer, J.O. Milewski, A.M. Beese, A. Wilson-Heid, A. De, W. Zhang, Progress in Materials Science 92 (2018) 112-224.

[2] Y.M. Wang, T. Voisin, J.T. McKeown, J. Ye, N.P. Calta, Z. Li, Z. Zeng, Y. Zhang, W. Chen, T.T. Roehling, R.T. Ott, M.K. Santala, P.J. Depond, M.J. Matthews, A.V. Hamza, T. Zhu, Nat Mater (2017).

[3] L. Liu, Q. Ding, Y. Zhong, J. Zou, J. Wu, Y.-L. Chiu, J. Li, Z. Zhang, Q. Yu, Z. Shen, Materials Today 21(4) (2018) 354-361.

[4] Z. Sun, X. Tan, S.B. Tor, C.K. Chua, NPG Asia Materials (2018).

[5] J.W. Yeh, S.K. Chen, S.J. Lin, J.Y. Gan, T.S. Chin, T.T. Shun, C.H. Tsau, S.Y. Chang, Advanced Engineering Materials 6(5) (2004) 299-303.

[6] B. Cantor, I.T.H. Chang, P. Knight, A.J.B. Vincent, Materials Science and Engineering: A 375-377 (2004) 213-218.

[7] B. Gludovatz, A. Hohenwarter, D. Catoor, E.H. Chang, E.P. George, R.O. Ritchie, Science 345(6201) (2014) 1153-1158.

[8] Z. Li, K.G. Pradeep, Y. Deng, D. Raabe, C.C. Tasan, Nature (2016).

[9] G. Salishchev, M. Tikhonovsky, D. Shaysultanov, N. Stepanov, A. Kuznetsov, I. Kolodiy, A. Tortika, O. Senkov, Journal of Alloys and Compounds 591 (2014) 11-21.

[10] W. Liu, J. He, H. Huang, H. Wang, Z. Lu, C. Liu, Intermetallics 60 (2015) 1-8.

[11] J.C. Rao, H.Y. Diao, V. Ocelík, D. Vainchtein, C. Zhang, C. Kuo, Z. Tang, W. Guo, J.D. Poplawsky, Y. Zhou, P.K. Liaw, J.T.M. De Hosson, Acta Materialia 131 (2017) 206-220.

[12] F. Otto, A. Dlouhý, C. Somsen, H. Bei, G. Eggeler, E.P. George, Acta Materialia 61(15) (2013) 5743-5755.

[13] Y. Brif, M. Thomas, I. Todd, Scripta Materialia 99 (2015) 93-96.

[14] R. Zhou, Y. Liu, C. Zhou, S. Li, W. Wu, M. Song, B. Liu, X. Liang, P. Liaw, Intermetallics 94 (2018) 165-171.

[15] Z.G. Zhu, Q.B. Nguyen, F.L. Ng, X.H. An, X.Z. Liao, P.K. Liaw, S.M.L. Nai, J. Wei, Scripta Materialia 154 (2018) 20-24.

[16] R. Li, P. Niu, T. Yuan, P. Cao, C. Chen, K. Zhou, Journal of Alloys and Compounds 746 (2018) 125-134.

[17] N.J. Harrison, I. Todd, K. Mumtaz, Acta Materialia 94 (2015) 59-68.

[18] Y. Chen, K. Zhang, J. Huang, S.R.E. Hosseini, Z. Li, Materials & Design 90 (2016) 586-594.

[19] E. Chauvet, P. Kontis, E.A. Jägle, B. Gault, D. Raabe, C. Tassin, J.-J. Blandin, R. Dendievel, B. Vayre, S. Abed, G. Martin, Acta Materialia 142 (2018) 82-94.

[20] J.H. Martin, B.D. Yahata, J.M. Hundley, J.A. Mayer, T.A. Schaedler, T.M. Pollock, Nature 549(7672) (2017) 365-369.

[21] T. Mukherjee, J. Zuback, A. De, T. DebRoy, Scientific reports 6 (2016).

[22] Z. Sun, X. Tan, S.B. Tor, W.Y. Yeong, Materials & Design 104 (2016) 197-204.

[23] F. Bachmann, R. Hielscher, H. Schaeben, Texture analysis with MTEX–free and open source software toolbox, Solid State Phenomena, Trans Tech Publ, 2010, pp. 63-68.

[24] Celik, G.A., Polat, S., Atapek, S.H, Haidemenopoulos, G.N., Archives of Foundry Engineering, 17(3), 163-167.

[25] S.-L. Chen, S. Daniel, F. Zhang, Y. Chang, X.-Y. Yan, F.-Y. Xie, R. Schmid-Fetzer, W. Oates, Calphad 26(2) (2002) 175-188.

[26] L. Thijs, K. Kempen, J.P. Kruth, J. Van Humbeeck, Acta Materialia 61, 2013, 1809-1819.

[27] P. Wang, B. Zhang, C.C. Tan, S. Raghavan, Y.F. Lim, C.N. Sun, J. Wei, D. Chi, Materials & Design, 2016, 290-299.

[28] X. Zhou, K. Li, D. Zhang, X. Liu, J. Ma, W, Liu, Z. Shen. Journal of Alloys and Compounds, 2015, 153-164.

[29] D, Wang, C. Yu, J. Ma, W. Liu, Z. Shen. Materials & Design, 2017, 44-52.

[30] M.A. Easton, M. Qian, A. Prasad, D.H. StJohn, Current Opinion in Solid State and Materials Science 20(1) (2016) 13-24.

[31] C.L.A. Leung, S. Marussi, R.C. Atwood, M. Towrie, P.J. Withers, P.D. Lee, Nat Commun 9(1) (2018) 1355.

[32] J.J. Lewandowski, M. Seifi, Annual Review of Materials Research 46 (2016) 151-186.

[33] S. Kou, Acta Materialia 88 (2015) 366-374.

[34] H. Yamamoto, S. Harada, T. Ueyama, S. Ogawa, F. Matsuda and K. Nakata, Welding International 7.6 (1993) 456-461.

[35] W. H. Suyitno, and L. Katgerman, Metallurgical and Materials Transactions A 36, (2005) 1537-1546.

[36] M. Rappaz, J.M. Drezet, M. Gremaud, Metallurgical and Materials Transactions A, 30(2) (2009) 449-455.

[37] N. Wang, S. Mokadem, M. Rappaz, W. Kurz, Acta Materialia, 52(11) (2004) 3173-3182.

[38] C. Hagenlocher, D. Weller, R. Weber, T. Graf. Science and Technology of Welding and Joining, (2018) 1-7.

[39] M.L.M. Sistiaga, R. Mertens, B. Vrancken, X. Wang, B. Van Hooreweder, J.P. Kruth, J. Van Humbeeck. Journal of Materials Processing Technology, 238 (2016), 437-445.

[40] M.L.M. Sistiaga, M.G. Marinez, K. Boschmans, J.P. Kruth, J. Van Humbeeck, K. Vanmeensel. Additive Manufacturing, 23 (2018) 402-410.

[41] M. Rappaz, J.A. Dantzig, EPFL Press. (2009)

[42] M. Mohr, R.K. Wunderlich, P.K. Liaw, L. Battezzati, H. Fecht. TMS2019 Proccedings.

Figure Captions

Figure 1. OM images of SLM-built HEA CoCrFeNi with (a) chessboard (denoted as C) and (b) stripe (denoted as S) scanning strategies. EBSD IPF color maps with respect to the build direction of the selected areas for (c) C sample and (d) S sample. Lack-of-fusion cracks and spherical pores are highlighted in black and red circles, respectively. Schematics of (e) chessboard and (f) stripe scanning strategies for SLM process.

Figure 2. μ-CT images with their corresponding cross-sectional OM images of the (a) C and (b) S samples. The chimney-like crack in C sample is circled in red dashed line. The tensile fracture surfaces of (c) C and (d) S samples with solidification cracks highlighted by white arrows. Enlarged view of solidification cracking for (e) C and (f) S samples showing typical smooth protrutions.

Figure 3. (a) SEM image showing that APT specimens were acquired on the periphery of a solidification crack. (b) SEM image showing an APT specimen tip with a dimension of ~50 nm. (c) APT reconstruction volumes showing atom distribution of the 4 constituting elements (Co, Cr, Fe and Ni).

Figure 4. (a) A generic schematic illustration of the solidification cracking mechanism in AM process. (b) TEM image showing a large number of dislocations within the as-built cellular microstructure. Cell boundaries are indicated by white arrows. A selected area diffraction (SAED) pattern is shown with a <1-10> zone axis. (c) Solidification paths of SS316L, CoCrFeNi and Al7075. (d) Hot tearing propensity with respect to their grain size and typical depression pressures for the chosen SLM-built alloys.

Figure(s)
Click here to download high resolution image

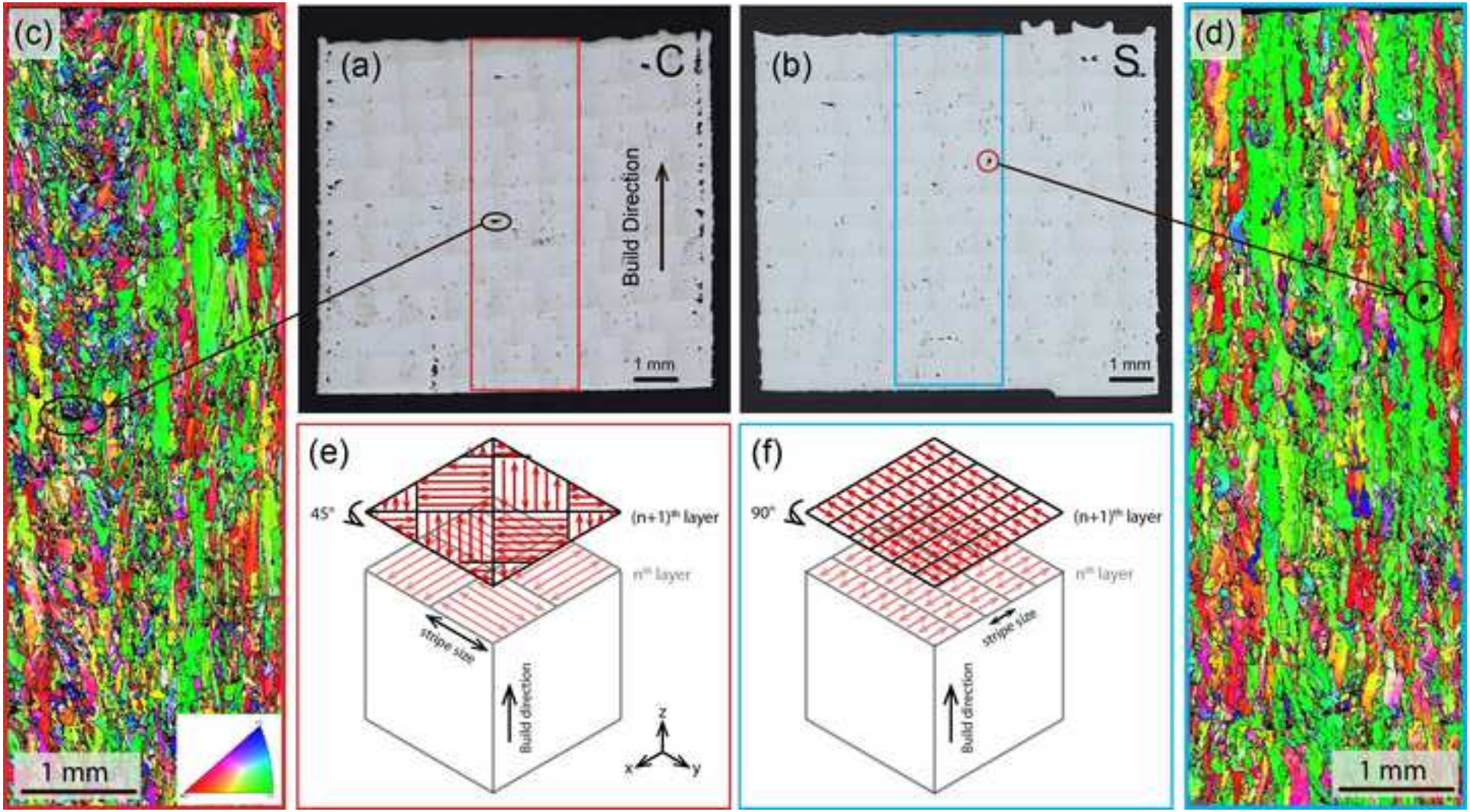

Figure(s)
Click here to download high resolution image

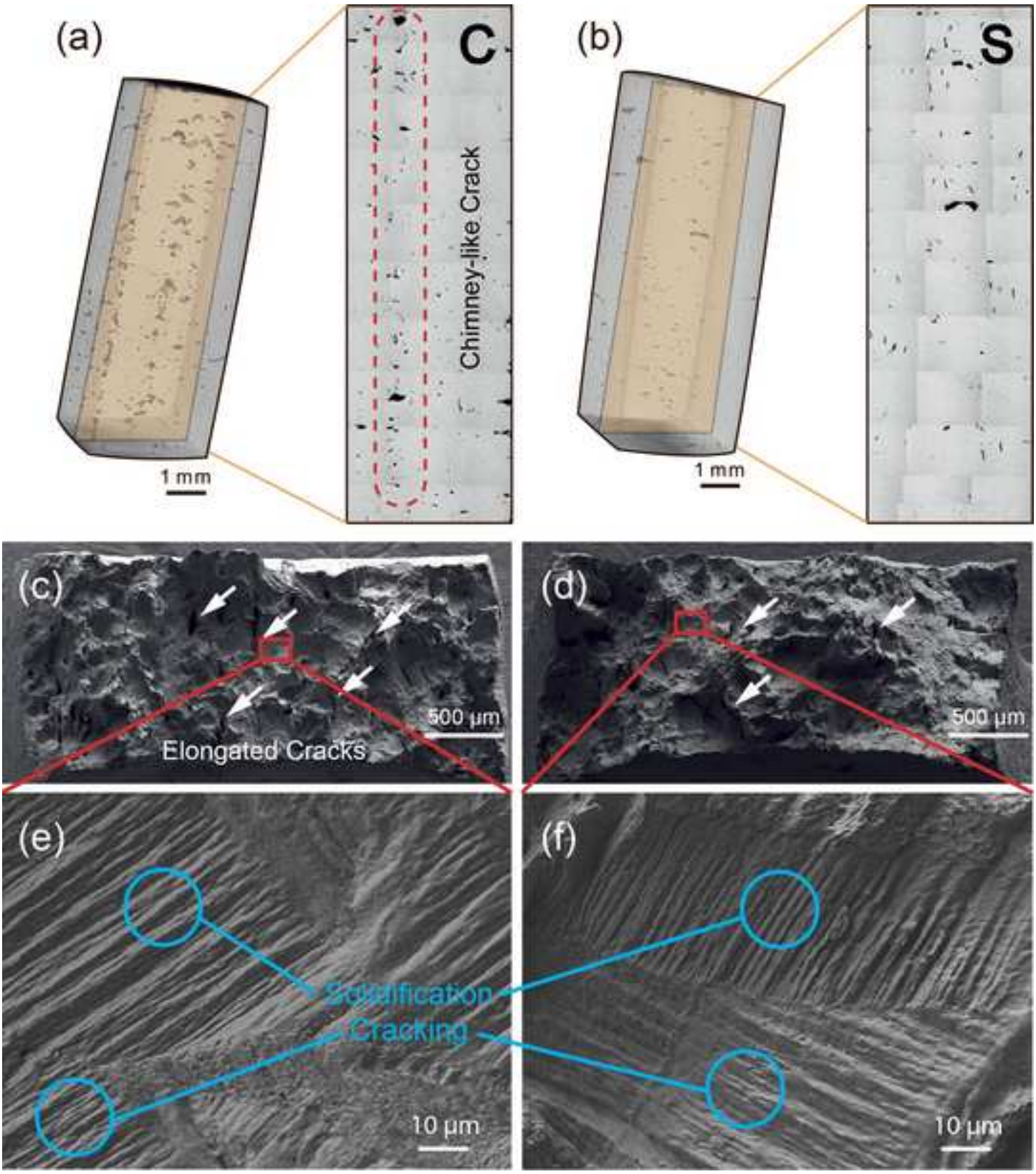

Figure(s)

Click here to download high resolution image

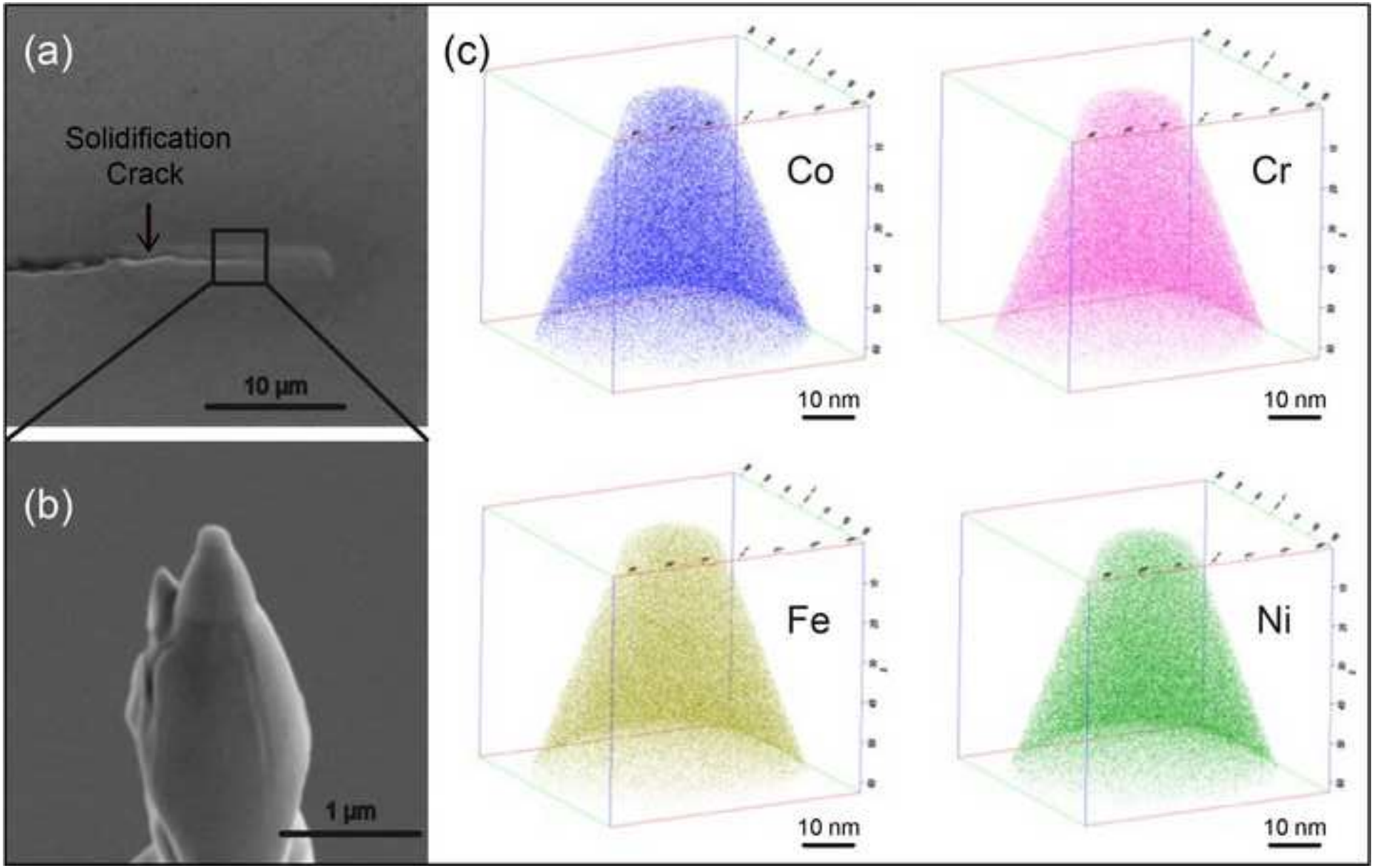

Figure(s)
Click here to download high resolution image

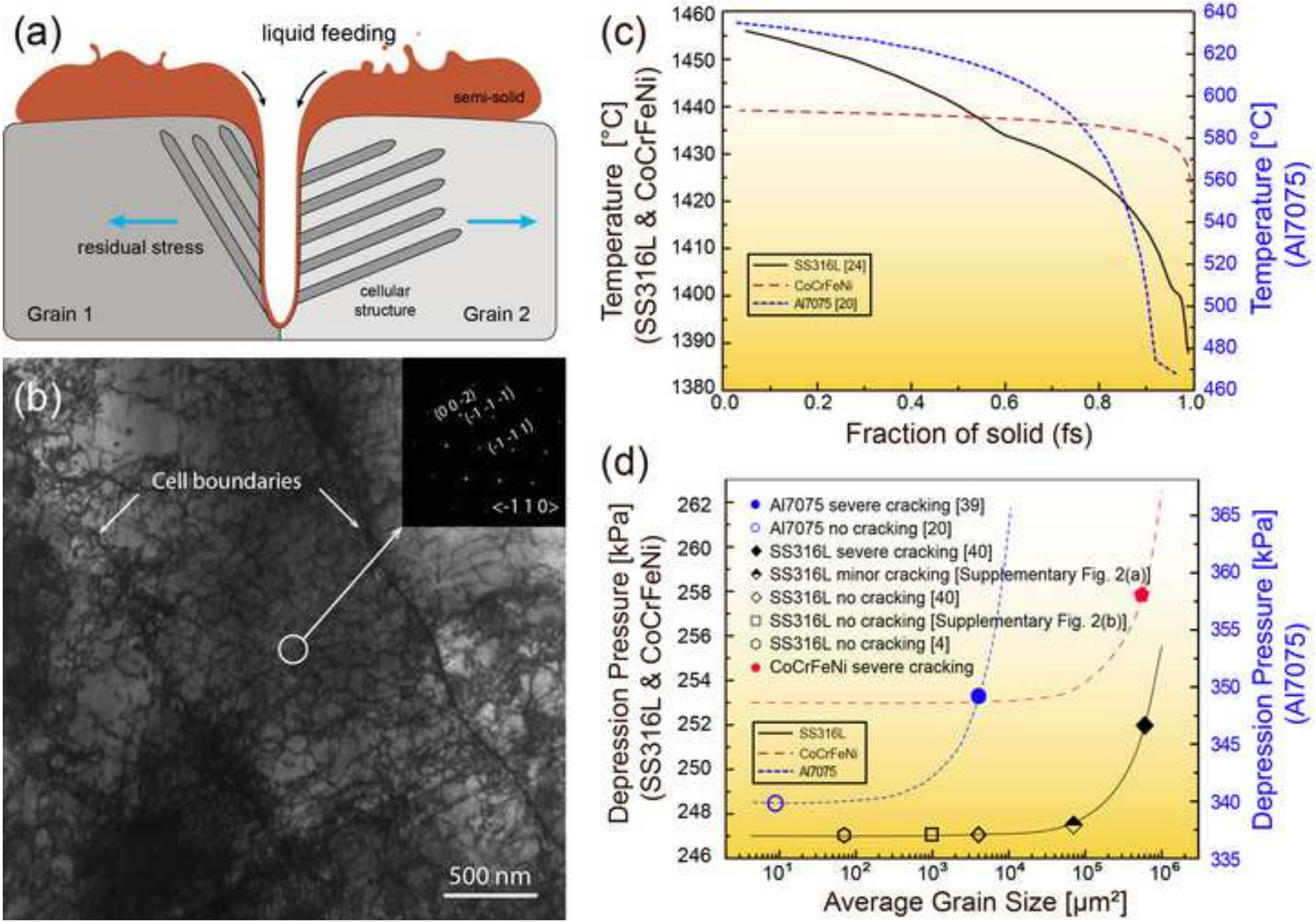

Supplementary Material

Click here to download Supplementary Material: Supplementary material.docx